Structural analysis of transient reaction intermediate in formic acid dehydrogenation catalysis using two-dimensional IR spectroscopy

Yufan Zhang[a,b,1], Xin Chen[a,1], Bin Zheng[c], Xunmin Guo[a,b], Yupeng Pan[c,d], Hailong Chen[a,b,2], Huaifeng Li[c,d], Shixiong Min[c,d], Chao Guan[c,d], Kuo-Wei Huang[c,d,3], and Junrong Zheng[a,3]

[a]College of Chemistry and Molecular Engineering, Beijing National Laboratory for Molecular Sciences, Peking University, 100871 Beijing, China; [b]Department of Chemistry, Rice University, Houston, TX 77005; [c]King Abdullah University of Science and Technology Catalysis Center, King Abdullah University of Science and Technology, 23955-6900 Thuwal, Saudi Arabia; and [d]Division of Physical Science and Engineering, King Abdullah University of Science and Technology , 23955-6900 Thuwal, Saudi Arabia

Edited by Michael D. Fayer, Stanford University, Stanford, CA, and approved October 29, 2018 (received for review May 31, 2018)

The molecular structure of a catalytically active key intermediate is determined in solution by employing 2D IR spectroscopy measuring vibrational cross-angles. The formate intermediate (2) in the formic acid dehydrogenation reaction catalyzed by a phosphorus–nitrogen PN^3P–Ru catalyst is elucidated. Our spectroscopic studies show that the complex features a formate ion directly attached to the Ru center as a ligand, and a proton added to the imine arm of the dearomatized PN^3P^* ligand. During the catalytic process, the imine arms are not only reversibly protonated and deprotonated, but also interacting with the protic substrate molecules, effectively serving as the local proton buffer to offer remarkable stability with a turnover number (TON) over one million.

formic acid dehydrogenation | vibrational cross-angle method | intermediate molecular structure

Identifying molecular structures of reaction intermediates is often the key to elucidate reaction mechanisms, which are indispensable for rational designs and optimization of catalytic systems in broad areas, including medicinal chemistry, industrial processes, and material science (1, 2). One of the most ideal approaches to study reaction intermediates is to first capture and then isolate them. In practice, however, reaction intermediates are often metastable and short-lived, making them very difficult or even impossible to isolate. It is challenging to resolve the molecular structures of these transient species in situ with traditional structural tools like X-ray crystallography and NMR techniques, due to their inherently low temporal resolutions. Two-dimensional IR (3–6), an ultrafast analog of 2D NMR, holds great promise to resolve structures of these transient species. It has been demonstrated that ultrafast dynamic and structural information can be obtained from 2D IR measurements for equilibrium systems and phototriggered reactions (7–15). However, the majority of chemical reactions on which most organic chemists work on a daily basis are thermally driven reactions. Their transient intermediates are yet to be explored by ultrafast laser spectroscopy. In this work, we apply a specially designed multiple-mode 2D IR technique that provides sufficiently high excitation power for resolving very weak vibrational cross-angle signals in reacting systems, to solve in situ the fast fluctuating conformation of a transient intermediate in a thermally driven reaction. The method relies on the fact that the ultrafast (femtosecond) resolution of the technique allows the determination of individual rapid-switching conformation rather than the average structure offered by a technique with temporal resolution slower than the switching dynamics.

The selective hydrogen generation reaction from the decomposition of formic acid catalyzed by a PN^3P^*–ruthenium pincer complex is chosen as the model reaction system (Fig. 1*A*) (16). Although hydrogen gas is considered to be an ideal fuel (17–22), using high-pressure gas tanks, the currently most practical method to store H_2, raises serious safety concerns in addition to low volumetric capacity. Formic acid (FA), a nontoxic and nonflammable liquid that could decompose reversibly into H_2 and CO_2 ($CO_2 + H_2 = HCOOH$), has been proposed as a hydrogen energy carrier (23–26). The forward and backward reactions together form a cycle of hydrogen storage and generation: In H_2 generation plants H_2 can be converted into FA for storage and transportation, and in places where H_2 is needed, FA can be decomposed into H_2 (27, 28). Notably, FA has a relatively high volumetric hydrogen capacity: 53 g H_2/L, corresponding with an energy density of 1.77 kW·h/L, making it a promising on-board storage solution for vehicles (29–33). Unsurprisingly, many research efforts have been devoted in developing both homogeneous and heterogeneous catalyst systems for the generation of H_2 from FA (24, 25, 33–58). However, when considering industry feasibility, many current catalytic systems face several challenges. Firstly, FA can decompose into either H_2 and CO_2 or H_2O and CO. The generation of CO cannot be avoided in many catalytic systems, and even a trace amount of CO generated could be fatal to the hydrogen fuel cells downstream. Secondly, the typical turnover numbers (TONs) achieved by those catalysts are not sufficiently large, often due to their sensitivity to air, water, and/or other impurities. Only a

Significance

We demonstrate that the transient intermediate structure, which is too fast for traditional techniques, e.g. NMR or X-ray diffraction, to resolve in a thermally driven reaction can be determined in situ with the vibrational cross-angle method. The principle of the method illustrated in the work is general for other organic reactions and the method is expected to bring profound impacts for the studies of chemical reactions. The reaction mechanism of a well-defined catalytic system with performance to generate H_2 from formic acid is elucidated.

Author contributions: Y.Z., K.-W.H., and J.Z. designed research; Y.Z., X.G., H.C., and J.Z. performed research; B.Z., Y.P., H.L., S.M., C.G., and K.-W.H. contributed new reagents/analytic tools; Y.Z., X.C., H.C., K.-W.H., and J.Z. analyzed data; and Y.Z., X.C., K.-W.H., and J.Z. wrote the paper.

The authors declare no conflict of interest.

This article is a PNAS Direct Submission.

Published under the PNAS license.

[1]Y.Z. and X.C. contributed equally to this work.

[2]Present address: Beijing National Laboratory for Condensed Matter Physics, CAS Key Laboratory of Soft Matter Physics, Institute of Physics, Chinese Academy of Sciences, 100190 Beijing, China.

[3]To whom correspondence may be addressed. Email: hkw@kaust.edu.sa or junrong@pku.edu.cn.

This article contains supporting information online at www.pnas.org/lookup/suppl/doi:10.1073/pnas.1809342115/-/DCSupplemental.

Published online November 19, 2018.

Downloaded from https://www.pnas.org by Peking University on September 3, 2022 from IP address 162.105.22.204.

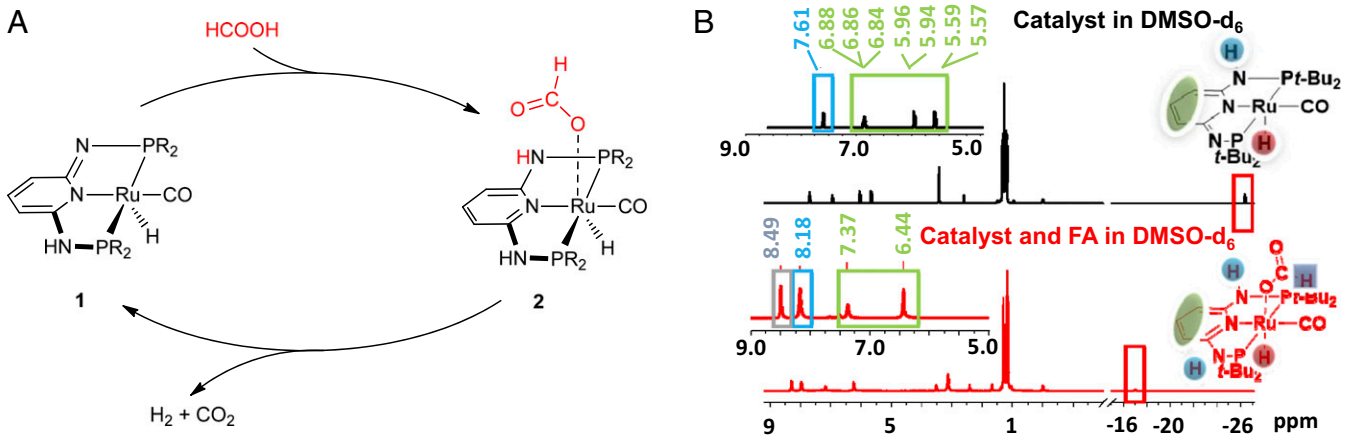

Fig. 1. (*A*) The decomposition of FA catalyzed by a PN^3P^*–pincer catalyst (1), the reactions going through a key intermediate (2); (*B*) ^1H NMR spectra of the catalyst **1** (*Upper*) and a mixture of the catalyst and FA (*Lower*), both in the solution of DMSO-d_6.

handful of examples of high TONs > 1,000,000 were reported (55, 58–61).

Our PN^3P^*–ruthenium pincer system can selectively generate hydrogen under mild conditions with no detectible CO. The highest turnover frequency (TOF) of >38,000 h^{-1} and TON of more than one million are achieved. Furthermore, the catalyst is air-stable and no noticeable catalytic activity loss was observed after aging in air for 1 mo (16). These properties are highly desirable in practical applications. In an effort to gain further insights into the unprecedented stability, we utilize 2D IR spectroscopy as a powerful tool to identify the molecular structure of an important intermediate in this highly efficient and promising catalytic reaction. The structure and conformation of the reaction intermediate (**2**) is determined, and the stability of our catalyst is rationalized together with density-functional (DFT) calculations.

Results and Discussion

NMR and FTIR Spectroscopies Support the Formation of a Ru Formate Complex (2). The catalytic system is first investigated with both NMR and FTIR spectroscopies. As we reported earlier (16), the comparison of the ^1H NMR spectra before and after addition of FA shows the generation of a species (Fig. 1*B*) that we rationalize to be a ruthenium formate complex. The three chemical shifts at δ 5.58 (d), 5.95 (d), and 6.86 (t) ppm for the three hydrogen atoms on the 3, 5, 4 positions of the pyridine ring, respectively, are typical for an unsymmetrical, dearomatizated pyridine ring. After adding FA (Fig. 1*B*, *Lower*), the proton signals shift downfield to δ 6.33 and 7.27 ppm. The two peaks at δ 5.95 ppm and 5.58 ppm in Fig. 1*B* (*Upper*) merge into the one that appears at δ 6.33 ppm. The area of this peak from these protons is now twice that of the peak at δ 7.27 ppm from the third proton on the same pyridine ring. In other words, two of the three protons on the pyridine ring become equivalent, indicating a Cs symmetry. Furthermore, the integration of the peak at δ 8.18 ppm for the NH groups is now twice that of a single H, clearly indicating that the imine group is protonated, resulting in a symmetrical and aromatized pyridine ring. Such a dearomatization/rearomatization process of the central pyridine ring through deprotonation/reprotonation of one of the *N*-H arms of the pincer complexes has been demonstrated to be a key step in the metal–ligand cooperative catalysis for a class of $PN^3(P)$–pincer systems (62).

The FTIR spectra shown in Fig. 2 feature five groups of bands between 1,350 and 2,250 cm^{-1}, each identified and attributed to five vibrational modes in the reactant or the catalyst, denoted as υ_1 to υ_5, and the corresponding modes in the additive complex, denoted as υ_1' to υ_5'. The assignments of these vibrational modes are listed in *SI Appendix*, Table S1. Herein, each mode will be briefly discussed, and they will be further interrogated in 2D IR spectroscopy to determine the structure and conformation of the catalyst/HCOOH complex, as elaborated in the next section.

First, the small absorption band at 2,113 cm^{-1} in Fig. 2 (*Inset*) (υ_1) belongs to the Ru–H stretch. As expected, such a feature is absent in pure HCOOH. In the catalyst/HCOOH mixture, however, its frequency decreases to 2,063 cm^{-1} and became υ_1'. The large redshift indicates that the Ru–H bond becomes weaker, which is expected when adding another *trans* ligand to the Ru center.

Second, the major absorption band at 1,940 cm^{-1} (υ_2) is attributed to the carbonyl ligand that is directly attached to Ru. With addition of HCOOH, its corresponding frequency in υ_2' increases for ∼15 cm^{-1}. Such a blueshift indicates a modest strengthening of the C≡O bond and therefore a weakening of the

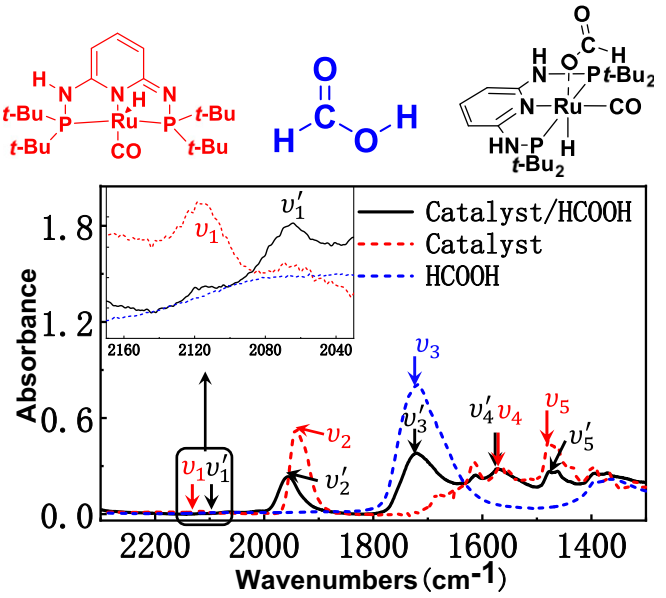

Fig. 2. FTIR spectra of the catalyst (red), the reactant (blue), and the mixture (black) in the frequency range from 1,200 to 2,400 cm^{-1}. (*Inset*) Zoomed-in FTIR spectra for the vibrational mode of Ru–H stretch in the catalyst and the reaction mixture (υ_1 and υ_1'), respectively.

Downloaded from https://www.pnas.org by Peking University on September 3, 2022 from IP address 162.105.22.204.

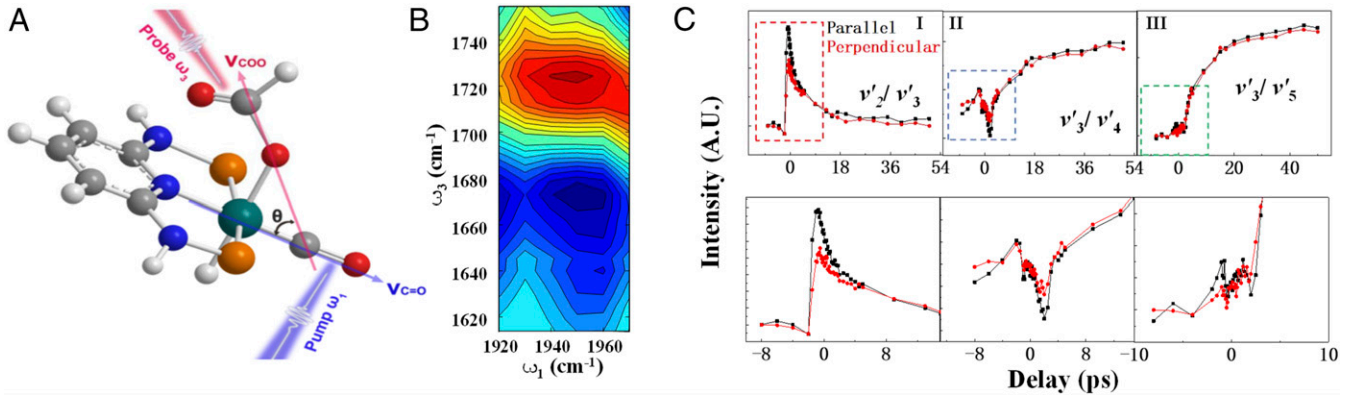

Fig. 3. Cross-peak measurements for vibrational mode pairs. (*A*) Illustrations of the cross-angle vibrational coupling measurement method for vibrational modes carbonyl stretch (v_2') and C=O stretch (v_3'). The t-butyl groups have been omitted for clarity. (*B*) The 2D spectrum of the cross-peak for v_2' and v_3' at a waiting time of 0.1 ps. (*C*) Plots of the polarization-dependent cross-peak intensities with the polarization of the excitation beam parallel (*//*) and perpendicular (⊥) to the polarization of the detection beam, respectively. (*Lower*) Enlarged figures of the early waiting time signals labeled on the upper panels.

metal–ligand interaction, which is again consistent with the notion of another ligand attaching to the Ru center.

Third, the major absorption band at 1,720 cm^{-1} (v_3) belongs to the C=O stretch from HCOOH. As expected, no such feature can be found on the catalyst itself. Interestingly, its corresponding frequency (v_3') remains virtually the same upon the formation of the complex. Such a frequency is very different from the carbonyl stretch in a free formate, where the C=O stretch mode would be completely delocalized on two oxygens and move to a much lower frequency (e.g., ∼1,620 cm^{-1} in sodium formate). The observed little-to-none frequency shift is consistent with formate binding as a ligand through a single Ru–oxygen bond, so that C=O remains largely localized. The lack of the frequency change further supports our conclusion that formate ion, rather than FA, serves as the ligand. If FA binds to Ru, it should be the oxygen of the C=O bond rather than the OH bond that attaches to Ru, which would immediately change the C=O vibrational frequency.

Lastly, the absorption bands at 1,450 cm^{-1} (v_4) and 1,615 cm^{-1} (v_5) undoubtedly belong to the symmetric and antisymmetric vibrational modes of the pyridine ring on the pincer ligand, respectively. Both v_4 and v_4', and v_5 and v_5' strongly overlap with each other. Apparently, they are not significantly affected by the formation of the complex. Consistent with the NMR results, FTIR spectra suggest that a formate ion, instead of a free FA, is bound to the Ru center as a ligand in the complex.

Although the above experimental observations are in good agreement with the formation of complex **2** with two NH arms and a formate ligand attached to Ru, they are not definitive and they do not provide information on the geometry which is critical for the understanding of reaction mechanism but fast fluctuates at the time scale of a few picoseconds (manifested by the anisotropy decay in Fig. 3*C*). During the catalytic reaction, **2** is observed as a transient species, and thus attempts to isolate **2** are in vain. However, as **2** is ligated by a well-defined and rigid PN^3P–pincer ligand, and the IR bands for the rest of three ligands, namely Ru–H, R–CO, and formate, are well distinguishable, 2D IR technique becomes suitable to elucidate the molecular structure of **2**.

Molecular Structure of Complex 2 Determined by 2D IR. In principle, the relative cross-angle between any two vibrational modes can be determined by measuring the anisotropy of the vibrational coupling between the two modes, i.e., the cross-peak in 2D IR spectroscopy if the instrument sensitivity is high enough. Briefly, the cross-peak measurement is illustrated in measurement schematic Fig. 3*A*. For example, the carbonyl stretch mode (v_2') on the catalyst is resonantly excited by a linearly polarized narrow-band IR pulse at about 1,955 cm^{-1} (ω_1 in Fig. 3*B*). Because of anharmonic coupling, the excitation of v_2' shifts the frequencies of other vibrational modes connected to it. The frequency change of the C=O vibrational mode (v_3') of formate caused by the excitation of v_2' is detected by another linearly polarized broad-band IR pulse from 1,610 to 1750 cm^{-1} after a period of waiting time of 0.1 ps. A 2D IR spectrum is plotted as the difference in the absorption of v_3' with v_2' excited and unexcited. The 2D spectrum in Fig. 3*B* features a cross-peak pair between vibrational modes v_2' and v_3' with the detection beam perpendicular to the excitation beam. A blue peak at $\omega_3 = 1{,}675$ cm^{-1} appears underneath a red peak at about 1,725 cm^{-1}. The red peak represents the vibrational absorption reduction at about 1,725 cm^{-1} caused by the v_2' excitation, while the blue peak shows the vibrational absorption increase at about 1,675 cm^{-1}. The results indicate that the vibrational excitation of the carbonyl stretch mode (v_2') of the catalyst shifts the C=O vibrational mode (v_3') of formate from about 1,725 cm^{-1} to about 1,675 cm^{-1}. The frequency shift of ∼50 cm^{-1} is much larger than that (∼6 cm^{-1}) of a vibrational pair bound through a H bond (63), suggesting that the binding between formate and the catalyst is even stronger than a typical H bond. Although the quantitative correlation between the anharmonicity shift and the interaction strength of vibrational pair is yet to be established, previous experimental observations suggest that a stronger interaction typically produces a larger frequency shift (64–70).

More importantly, the signal amplitudes of the cross-peaks in 2D IR depend on the relative polarizations of the excitation and detection pulses and the directions of transition dipole moments of the involved vibrational modes (66, 71). For an isotropically distributed sample within the laser focus spot (diameter ∼ 150 μm), the vibrational cross-angle between the transition dipole moments of the involved vibrational modes can be directly determined using the equation (72, 73)

$$\frac{I_{\perp}}{I_{//}} = \frac{2 - \overline{\cos^2\theta}}{1 + 2\overline{\cos^2\theta}}, \qquad [1]$$

where $I_{\perp}$ and $I_{//}$ are the signal intensities for parallel and perpendicular measurements, respectively, taken at very short waiting times before any molecular rotation or conformational changes can happen for a substantial extent. The vibrational cross-angles can then be converted into 3D molecular conformations (66). To exclude the interference from the free catalyst and FA in the mixed system, all signals are collected from exciting vibrational modes on the catalyst part of the complex and detecting the responses on the formate part, or vice versa. The time-dependent polarization-selective signals for different vibrational

Downloaded from https://www.pnas.org by Peking University on September 3, 2022 from IP address 162.105.22.204.

Table 1. Vibrational cross-angles experimentally determined

Cross-peak	Modes	Angle, θ
I	ν'_1/ν'_3	57° ± 4°
II	ν'_2/ν'_3	45° ± 5°
III	ν'_3/ν'_4	45° ± 6°
IV	ν'_3/ν'_5	51° ± 9°

mode pairs are displayed in Fig. 3*C*. The signal dynamic time constants are within 10 ps. This fast decay is most likely because of the wobbling of formate of the complex, because the complex is too bulky to rotate so fast and intermolecular energy transfers should be much slower (74). The cross-angles between vibrational mode pairs are listed in Table 1, which are derived from the signal intensities by applying Eq. **1** (75).

It is important to note that some vibrational modes involved in the above measurements are delocalized in the complex; the direction of the transition dipole moments of the vibrational modes are closely related to, but not necessarily the same as, those of the chemical bonds. There is no direct method to identify a conformation from a set of vibrational angles. However, the reverse can be achieved; each conformation must feature a unique set of vibrational cross-angles, which can be calculated individually using ab initio method (66). We therefore define the most likely conformation as the one that minimizes the overall difference between the experimental and calculated vibrational cross-angles, according to the following equation:

$$E_r = \frac{\sum_{i=1}^{m} |A_i^C - A_i^E|}{m}, \qquad [2]$$

where E_r is the averaged deviation value; A_i^C is the calculated vibrational cross-angle of the *i*th pair of vibrational normal modes of a certain molecular conformation; A_i^E is the experimentally obtained vibrational cross-angle of the *i*th pair of normal modes (as listed in Table 1); the absolute sign represents the difference between the two angles in the circular fashion; and *m* is the number of pairs compared.

For this complex particularly, we explore the conformational space by rotating the formate along the two single bonds: the Ru–O1 bond that connects the metal center and ligand, and the C2–O2 bond next to the Ru–O bond. These two degrees of freedom are essentially the tilt angle and twist angle of the formate ion relative to the pyridine ring. In total, we search 576 possible conformations by varying the dihedral angle C1(CO)–Ru–O1–C2 from −5° to 175° for every 10° and Ru–O1–C2–O2 from 1° to 351° for every 10°. The vibrational cross-angles for each conformation are calculated and then compared with the measured one according to Eq. **2**. The E_r values are plotted in Fig. 4*A*. The minimum E_r value is found at the dihedral angles (Ru–O1–C2–O2, C1–Ru–O1–C2) (321°, 155°) at the northeastern corner of the map. The corresponding conformation of the catalyst/formate complex is displayed in Fig. 4*B*.

Insights from the Conformational Analysis. The molecular structure of formate species **2** determined by the 2D IR is very intriguing, because DFT calculations indeed suggest a different structure as the global minimum (**2′**) among all conformers (Fig. 5). Both structures show similar PN^3P–pincer framework but different orientation of the coordinated formate group. Structure **2′** was computed to be 1.2 (3.8) kcal/mol more stable than **2** [energy in the Polarizable Continuum Model (PCM) in parentheses; see *SI Appendix* for details], presumably due to the relief from the electron–electron repulsion between the formate ligand and the pyridine ring. These observations strongly suggest the existence of certain driving force to allow complex **2** to stay in an apparently more strained conformation.

In light of the 2D IR structure, our hypothesis is that there may be a protic molecule (H_2O or HCOOH) bridging the carbonyl oxygen of the formate ligand and the proton of one of the *N*-H arms. To our delight, the fully optimized structure of complex **2** containing either one water molecule (**2-W**) or one FA (**2-FA**) shows a very similar geometry of the formate group to that of **2** (Fig. 6). Moreover, the formation of **2-W** and **2-FA** is found energetically favorable by 6.5 (8.6) (compared with **2′** and H_2O, energy in the PCM in parentheses; see *SI Appendix* for details) and 4.8 (9.6) kcal/mol (compared with **2′** and HCOOH), respectively. These findings imply that the *N*-H arms of the PN^3P–Ru catalyst can play a role to interact with the protic molecules in the reaction mixture in addition to mediating the dearomatization/rearomatization of the central pyridine ring for FA

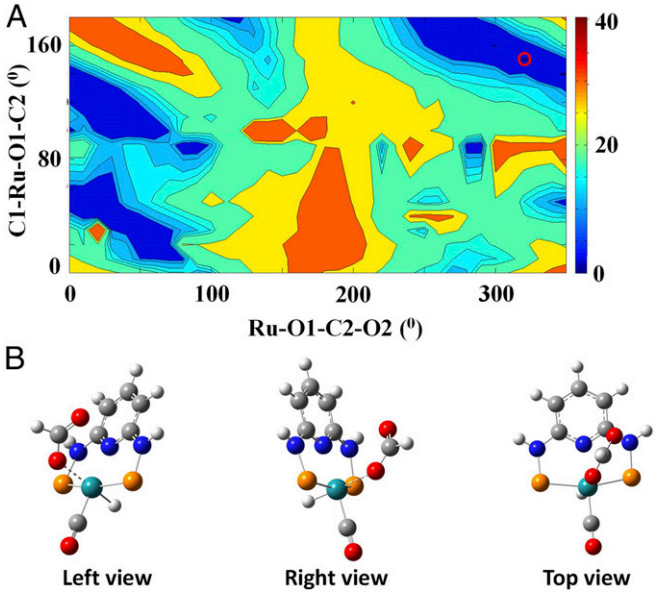

Fig. 4. Determine the conformation of complex **2**. (*A*) The difference (E_r) between experimental and calculated vibrational cross-angles for 576 possible conformations of with different Ru–O1–C2–O2 and C1–Ru–O1–C2 dihedral angles. The *z* axis is the value of E_r shown in a color map. (*B*) The most stable conformation (red circle in Fig. 4*A*) from different views. The butyl groups are omitted for clarity.

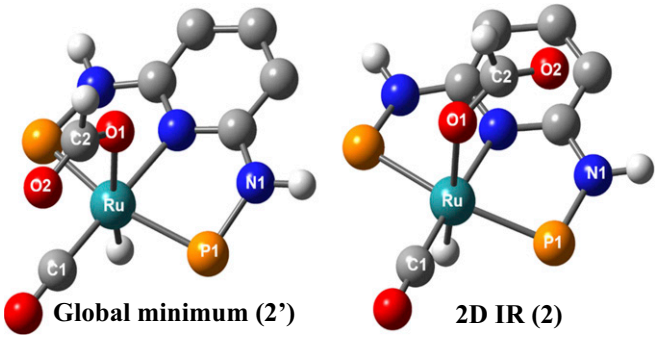

Fig. 5. Comparison of the global minimum (**2′**) and "optimized" 2D-IR (**2**) structures of complex **2**. Key geometrical parameters (Å and °): **2**: Ru–C1 1.847, Ru–O1 2.259, Ru–P1 2.330, C1–Ru–O1–C2 147.53; **2′**: Ru–C1 1.858, Ru–O1 2.235, Ru–P1 2.341, C1–Ru–O1–C2 −3.50. The butyl groups are omitted for clarity.

Downloaded from https://www.pnas.org by Peking University on September 3, 2022 from IP address 162.105.22.204.

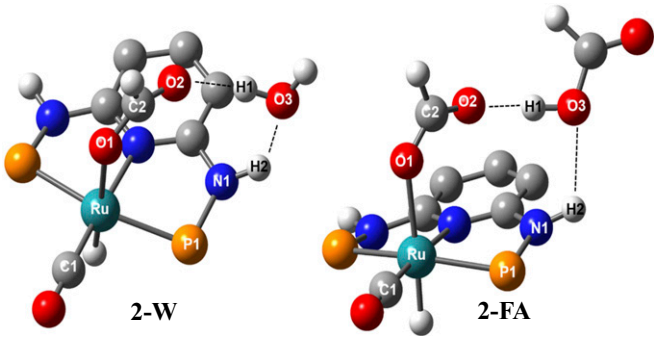

Fig. 6. Computed structures of **2·H_2O** (**2-W**) and **2·HCOOH** (**2-FA**). Key geometrical parameters (Å and °): **2-W** Ru–C1 1.848, Ru–O1 2.296, Ru–P1 2.339, O2–H1 1.771, O3–H2 1.998, C1–Ru–O1–C2 152.96; **2-FA** Ru–C1 1.850, Ru–O1 2.302, Ru–P1 2.338, O2–H1 1.613, O3–H2 2.302, C1–Ru–O1–C2 156.65. The butyl groups are omitted for clarity.

decomposition and hydrogen generation processes. The formate–water (FA)–NH ring structure (**2-W** and **2-FA**) is very interesting and may be one important reason responsible for the excellent stability of the catalyst. It forms an effective polar screen on the top of the N1 and P1 atoms, which can reduce their probability of being attacked by ions or polar molecules, e.g., protonated water, and thus minimize the decompositions of the *N*–P and P–Ru bonds. We want to emphasize that the formate–water–NH hydrogen and formate–FA–NH hydrogen bonds proposed here are only representative examples to form such a ring structure. The water or HCOOH molecule can be any protic species in the reaction.

Concluding Remarks

In summary, we have demonstrated that the structure of a key reactive intermediate in a thermally driven hydrogen generation reaction can be resolved by 2D IR spectroscopy using the ultrafast vibrational cross-angle method. The results from the ultrafast vibrational measurements and NMR results suggest that the NH arms of the PN^3P–pincer Ru catalyst indeed interact with the protic environments, namely playing a role as the local buffer. This may facilitate the reaction by stabilizing the additive complex and also significantly reduce the chance of free proton directly attacking the metal center and other coordination atoms, minimizing decomposition of the catalyst. These are likely the contributing factors for this catalytic system with high reactivity and stability, as evident in its high TOF and TON values. Very importantly, our work demonstrates that the high-powered ultrafast vibrational cross-angle measurement holds great promise to resolve the transient intermediate structures in situ, which are difficult to study with traditional techniques due to their fast dynamics, and this technique holds a great promise for mechanistic study in catalysis.

Materials and Methods

Synthesis and Sample Preparation. $RuPN^3P$ was synthesized by adding a solution of Ru_1 (47 mg, 0.05 mmol) in THF (10 mL) dropwise to a ligand $^tBu_2PN^3P$ (20 mg, 0.05 mmol) in THF (4 mL) and heated at 65 °C for 12 h. $RuPN^3P$ (281.6 mg, 0.5 mmol) was dissolved in THF (4 mL). A solution of KO^tBu (56.0 mg, 0.5 mmol) in THF (4 mL) was added to it and the reaction mixture was stirred at room temperature for 2 h. The solvent was then removed under vacuum and washed with hexane (1 mL × 3) and dried under vacuum to obtain the catalyst. All reactions were conducted under argon protection. FA was purchased from Sigma-Aldrich and used as received. For the FTIR and vibrational cross-angle measurements, catalyst 1 and FA were mixed with a molar ratio of 1:4 and sealed in a cell with CaF_2 windows. During the ultrafast spectroscopic measurements, hydrogen was constantly generated from the decomposition of FA. More experimental details are provided in *SI Appendix*.

NMR Experiments. For ^{1}H-NMR and NOESY experiments, HCOOH (1.62 mg) was added into a DMSO-d_6 (0.5 mL) solution of 1 (20.2 mg) in a screw-capped NMR tube at room temperature. Reaction was observed by visual inspection.

Optical Experiments. The optical setup used is described in detail in our previous publication (66). The oscillator provides the same seed pulse for a picosecond (ps) amplifier and a femtosecond (fs) amplifier (UpTek Solution Corp.) which are synchronized. The ps amplifier pumps an optical parametric amplifier to produce ∼0.8 ps (would vary from 0.7 ∼0.9 ps in different frequencies) mid-IR pulses with a bandwidth 10 ∼35 cm^{-1} in a tunable frequency range from 400 to 4,000 cm^{-1} with energy 1∼40 μJ/pulse (1∼10-μJ/pulse for 400–900 cm^{-1} and >10-μJ/pulse for higher frequencies) at 1 kHz. The bandwidth is narrower at a longer wavelength. At 2,000 cm^{-1}, the bandwidth is about 18 cm^{-1}. The detailed characterization of the outputs of the laser systems can be found in our previous work (73). This ps IR pulse is used as excited pulse in the cross-coupling experiments. The fs amplifier is used to generate a high-intensity mid-IR and terahertz supercontinuum pulse with a pulse duration around 110 fs in the frequency range from <20 to >3,500 cm^{-1} at 1 kHz, and the shot-to-shot fluctuation is less than 1% in most of the spectral region. This supercontinuum pulse is used as the detection pulse, which is frequency-resolved by a spectrograph. More details are provided in *SI Appendix*.

Theoretical Computations. Computations on nonmetal elements were performed by employing the program suite Gaussian 09, using DFT with Truhlar's hybrid metaexchange-correlation functional M06 (76) in conjunction with a 6–31G(d,p) basis set. For Ru atom, Stuttgart–Dresden effective core potentials (77) were used. To generate all of the possible structures, we preset 576 possible conformations for intermediate **2** by varying the dihedral angle C1–Ru–O1–C2 from −5° to 175° for every 10° and Ru–O1–C2–O2 from 1° to 351° for every 10°. Each structure with different pair of dihedral angles fixed is optimized under the computational method described above. The optimized structures of **2**, **2′**, **2-W**, and **2-FA** were characterized by frequency calculations. Solvent effects were estimated by performing a single point calculation at the same level of theory using the PCM with the integral equation formalism variant (78) in H_2O (a continuum solvent dielectric of ε = 78.3553) and DMSO (a continuum solvent dielectric of ε = 46.826).

ACKNOWLEDGMENTS. Y.Z. acknowledges a Schlumberger future faculty award. This work is supported by National Natural Science Foundation of China (NSFC) (NSFC-21627805, 21673004, and 21821004), NSF (CHE-1503865), and Ministry of Science and Technology of the People's Republic of China (2017YFA0204702) (to J.Z.), and by King Abdullah University of Science and Technology (to K.-W.H.).

1. Milo A, Neel AJ, Toste FD, Sigman MS (2015) Organic chemistry. A data-intensive approach to mechanistic elucidation applied to chiral anion catalysis. *Science* 347: 737–743.
2. Ananikov VP (2014) *Understanding Organometallic Reaction Mechanisms and Catalysis: Computational and Experimental Tools* (John Wiley & Sons, New York).
3. Mukamel S (1995) *Principles of Nonlinear Optical Spectroscopy* (Oxford Univ Press, New York).
4. Tanimura Y, Mukamel S (1993) Two-dimensional femtosecond vibrational spectroscopy of liquids. *J Chem Phys* 99:9496–9511.
5. Hamm P, Lim M, Hochstrasser RM (1998) Structure of the Amide I band of peptides measured by femtosecond nonlinear-infrared spectroscopy. *J Phys Chem B* 102: 6123–6138.
6. Khalil M, Demirdoven N, Tokmakoff A (2003) Coherent 2D IR spectroscopy: Molecular structure and dynamics in solution. *J Phys Chem A* 107:5258–5279.
7. van Wilderen LJ, Messmer AT, Bredenbeck J (2014) Mixed IR/Vis two-dimensional spectroscopy: Chemical exchange beyond the vibrational lifetime and sub-ensemble selective photochemistry. *Angew Chem Int Ed Engl* 53:2667–2672.
8. Bredenbeck J, Helbing J, Hamm P (2004) Labeling vibrations by light: Ultrafast transient 2D-IR spectroscopy tracks vibrational modes during photoinduced charge transfer. *J Am Chem Soc* 126:990–991.
9. Donaldson PM, Hamm P (2013) Gold nanoparticle capping layers: Structure, dynamics, and surface enhancement measured using 2D-IR spectroscopy. *Angew Chem Int Ed Engl* 52:634–638.
10. Kurochkin DV, Naraharisetty SRG, Rubtsov IV (2007) A relaxation-assisted 2D IR spectroscopy method. *Proc Natl Acad Sci USA* 104:14209–14214.
11. Baiz CR, McRobbie PL, Anna JM, Geva E, Kubarych KJ (2009) Two-dimensional infrared spectroscopy of metal carbonyls. *Acc Chem Res* 42:1395–1404.
12. Slenkamp KM, et al. (2014) Investigating vibrational anharmonic couplings in cyanide-bridged transition metal mixed valence complexes using two-dimensional infrared spectroscopy. *J Chem Phys* 140:084505.
13. Maekawa H, De Poli M, Toniolo C, Ge NH (2009) Couplings between peptide linkages across a 3(10)-helical hydrogen bond revealed by two-dimensional infrared spectroscopy. *J Am Chem Soc* 131:2042–2043.

Downloaded from https://www.pnas.org by Peking University on September 3, 2022 from IP address 162.105.22.204.

14. Mukamel S (1990) Femtosecond optical spectroscopy: A direct look at elementary chemical events. *Annu Rev Phys Chem* 41:647–681.
15. Zhang WM, Chernyak V, Mukamel S (1999) Multidimensional femtosecond correlation spectroscopies of electronic and vibrational excitons. *J Chem Phys* 110: 5011–5028.
16. Pan Y, et al. (2016) Selective hydrogen generation from formic acid with well-defined complexes of ruthenium and phosphorus-nitrogen PN(3) -pincer ligand. *Chem Asian J* 11:1357–1360.
17. Lewis NS, Nocera DG (2006) Powering the planet: Chemical challenges in solar energy utilization. *Proc Natl Acad Sci USA* 103:15729–15735.
18. Whitesides GM, Crabtree GW (2007) Don't forget long-term fundamental research in energy. *Science* 315:796–798.
19. Moriarty P, Honnery D (2009) Hydrogen's role in an uncertain energy future. *Int J Hydrogen Energy* 34:31–39.
20. Moriarty P, Honnery D (2010) A hydrogen standard for future energy accounting? *Int J Hydrogen Energy* 35:12374–12380.
21. Turner JA (2004) Sustainable hydrogen production. *Science* 305:972–974.
22. Armaroli N, Balzani V (2011) The hydrogen issue. *ChemSusChem* 4:21–36.
23. Masel R (2006) Energy technology: Hydrogen quick and clean. *Nature* 442:521–522.
24. Hull JF, et al. (2012) Reversible hydrogen storage using CO2 and a proton-switchable iridium catalyst in aqueous media under mild temperatures and pressures. *Nat Chem* 4:383–388.
25. Tedsree K, et al. (2011) Hydrogen production from formic acid decomposition at room temperature using a Ag-Pd core-shell nanocatalyst. *Nat Nanotechnol* 6:302–307.
26. Eppinger J, Huang KW (2017) Formic acid as a hydrogen energy carrier. *ACS Energy Lett* 2:188–195.
27. Fellay C, Dyson PJ, Laurenczy G (2008) A viable hydrogen-storage system based on selective formic acid decomposition with a ruthenium catalyst. *Angew Chem Int Ed Engl* 47:3966–3968.
28. Loges B, Boddien A, Junge H, Beller M (2008) Controlled generation of hydrogen from formic acid amine adducts at room temperature and application in H2/O2 fuel cells. *Angew Chem Int Ed Engl* 47:3962–3965.
29. Felderhoff M, Weidenthaler C, von Helmolt R, Eberle U (2007) Hydrogen storage: The remaining scientific and technological challenges. *Phys Chem Chem Phys* 9: 2643–2653.
30. Sakintuna B, Lamari-Darkrim F, Hirscher M (2007) Metal hydride materials for solid hydrogen storage: A review. *Int J Hydrogen Energy* 32:1121–1140.
31. Yueruem Y, Taralp A, Veziroglu TN (2009) Storage of hydrogen in nanostructured carbon materials. *Int J Hydrogen Energy* 34:3784–3798.
32. Suh MP, Park HJ, Prasad TK, Lim D-W (2012) Hydrogen storage in metal-organic frameworks. *Chem Rev* 112:782–835.
33. Boddien A, et al. (2010) Iron-catalyzed hydrogen production from formic acid. *J Am Chem Soc* 132:8924–8934.
34. Fukuzumi S, Kobayashi T, Suenobu T (2008) Efficient catalytic decomposition of formic acid for the selective generation of H2 and H/D exchange with a water-soluble rhodium complex in aqueous solution. *ChemSusChem* 1:827–834.
35. Zhou X, et al. (2008) *High-Quality Hydrogen from the Catalyzed Decomposition of Formic Acid by Pd-Au/C and Pd-Ag/C* (Chemical Communications, Cambridge, UK), pp 3540–3542.
36. Boddien A, et al. (2009) Continuous hydrogen generation from formic acid: Highly active and stable ruthenium catalysts. *Adv Synth Catal* 351:2517–2520.
37. Ojeda M, Iglesia E (2009) Formic acid dehydrogenation on au-based catalysts at near-ambient temperatures. *Angew Chem Int Ed Engl* 48:4800–4803.
38. Ting S-W, Cheng S, Tsang K-Y, van der Laak N, Chan K-Y (2009) *Low Activation Energy Dehydrogenation of Aqueous Formic Acid on Platinum-Ruthenium-Bismuth Oxide at Near Ambient Temperature and Pressure* (Chemical Communications, Cambridge, UK), pp 7333–7335.
39. Himeda Y (2009) Highly efficient hydrogen evolution by decomposition of formic acid using an iridium catalyst with 4,4′-dihydroxy-2,2′-bipyridine. *Green Chem* 11: 2018–2022.
40. Bulushev DA, Beloshapkin S, Ross JRH (2010) Hydrogen from formic acid decomposition over Pd and Au catalysts. *Catal Today* 154:7–12.
41. Huang Y, Zhou X, Yin M, Liu C, Xing W (2010) Novel PdAu@Au/C core-shell catalyst: Superior activity and selectivity in formic acid decomposition for hydrogen generation. *Chem Mater* 22:5122–5128.
42. Scholten JD, Prechtl MHG, Dupont J (2010) Decomposition of formic acid catalyzed by a phosphine-free ruthenium complex in a task-specific ionic liquid. *ChemCatChem* 2: 1265–1270.
43. Majewski A, Morris DJ, Kendall K, Wills M (2010) A continuous-flow method for the generation of hydrogen from formic acid. *ChemSusChem* 3:431–434.
44. Zhou X, et al. (2010) Available hydrogen from formic acid decomposed by rare earth elements promoted Pd-Au/C catalysts at low temperature. *ChemSusChem* 3: 1379–1382.
45. Boddien A, et al. (2011) Efficient dehydrogenation of formic acid using an iron catalyst. *Science* 333:1733–1736.
46. Solymosi F, Koos A, Liliom N, Ugrai I (2011) Production of CO-free H2 from formic acid. A comparative study of the catalytic behavior of Pt metals on a carbon support. *J Catal* 279:213–219.
47. Tanaka R, Yamashita M, Chung LW, Morokuma K, Nozaki K (2011) Mechanistic studies on the reversible hydrogenation of carbon dioxide catalyzed by an Ir-PNP complex. *Organometallics* 30:6742–6750.
48. Luo Q, Feng G, Beller M, Jiao H (2012) Formic acid dehydrogenation on Ni(111) and comparison with Pd(111) and Pt(111). *J Phys Chem C* 116:4149–4156.
49. Mori K, Dojo M, Yamashita H (2013) Pd and Pd-Ag nanoparticles within a macroreticular basic resin: An efficient catalyst for hydrogen production from formic acid decomposition. *ACS Catal* 3:1114–1119.
50. Gan W, Snelders DJM, Dyson PJ, Laurenczy G (2013) Ruthenium(II)-catalyzed hydrogen generation from formic acid using cationic, ammoniomethyl-substituted triarylphosphine ligands. *ChemCatChem* 5:1126–1132.
51. Wang Z-L, et al. (2013) An efficient CoAuPd/C catalyst for hydrogen generation from formic acid at room temperature. *Angew Chem Int Ed Engl* 52:4406–4409.
52. Wang Z-L, Yan J-M, Wang H-L, Ping Y, Jiang Q (2013) Au@Pd core-shell nanoclusters growing on nitrogen-doped mildly reduced graphene oxide with enhanced catalytic performance for hydrogen generation from formic acid. *J Mater Chem A* 1: 12721–12725.
53. Zell T, Butschke B, Ben-David Y, Milstein D (2013) Efficient hydrogen liberation from formic acid catalyzed by a well-defined iron pincer complex under mild conditions. *Chemistry* 19:8068–8072.
54. Oldenhof S, et al. (2013) Base-free production of H2 by dehydrogenation of formic acid using an iridium-bisMETAMORPhos complex. *Chemistry* 19:11507–11511.
55. Sponholz P, Mellmann D, Junge H, Beller M (2013) Towards a practical setup for hydrogen production from formic acid. *ChemSusChem* 6:1172–1176.
56. Filonenko GA, et al. (2013) The impact of metal–ligand cooperation in hydrogenation of carbon dioxide catalyzed by ruthenium PNP pincer. *ACS Catal* 3:2522–2526.
57. Bielinski EA, et al. (2014) Lewis acid-assisted formic acid dehydrogenation using a pincer-supported iron catalyst. *J Am Chem Soc* 136:10234–10237.
58. Wang Z, Lu SM, Li J, Wang J, Li C (2015) Unprecedentedly high formic acid dehydrogenation activity on an iridium complex with an N,N′-diimine ligand in water. *Chemistry* 21:12592–12595.
59. Onishi N, et al. (2016) Direction to practical production of hydrogen by formic acid dehydrogenation with Cp*Ir complexes bearing imidazoline ligands. *Catal Sci Technol* 6:988–992.
60. Iguchi M, Himeda Y, Manaka Y, Matsuoka K, Kawanami H (2016) Simple continuous high-pressure hydrogen production and separation system from formic acid under mild temperatures. *ChemCatChem* 8:886–890.
61. Celaje JJA, et al. (2016) A prolific catalyst for dehydrogenation of neat formic acid. *Nat Commun* 7:11308.
62. Li H, Zheng B, Huang K-W (2015) A new class of PN3-pincer ligands for metal–ligand cooperative catalysis. *Coord Chem Rev* 293–294:116–138.
63. Bian HT, Li JB, Wen XW, Zheng JR (2010) Mode-specific intermolecular vibrational energy transfer. I. Phenyl selenocyanate and deuterated chloroform mixture. *J Chem Phys* 132:184505.
64. Naraharisetty SRG, Kasyanenko VM, Rubtsov IV (2008) Bond connectivity measured via relaxation-assisted two-dimensional infrared spectroscopy. *J Chem Phys* 128: 104502.
65. Bian H, Wen X, Li J, Zheng J (2010) Mode-specific intermolecular vibrational energy transfer. II. Deuterated water and potassium selenocyanate mixture. *J Chem Phys* 133: 034505.
66. Chen H, et al. (2013) Vibrational cross-angles in condensed molecules: A structural tool. *J Phys Chem A* 117:8407–8415.
67. Bian H, et al. (2011) Mapping molecular conformations with multiple-mode two-dimensional infrared spectroscopy. *J Phys Chem A* 115:3357–3365.
68. Naraharisetty SRG, Kurochkin DV, Rubtsov IV (2007) C-D modes as structural reporters via dual-frequency 2DIR spectroscopy. *Chem Phys Lett* 437:262–266.
69. Rubtsov IV (2009) Relaxation-assisted two-dimensional infrared (RA 2DIR) method: Accessing distances over 10 A and measuring bond connectivity patterns. *Acc Chem Res* 42:1385–1394.
70. Kasyanenko VM, Tesar SL, Rubtsov GI, Burin AL, Rubtsov IV (2011) Structure dependent energy transport: Relaxation-assisted 2DIR measurements and theoretical studies. *J Phys Chem B* 115:11063–11073.
71. Zanni MT, Asplund MC, Hochstrasser RM (2001) Two-dimensional heterodyned and stimulated infrared photon echoes of N-methylacetamide-D. *J Chem Phys* 114:4579.
72. Lakowicz J (2006) *Principles of Fluorescence Spectroscopy* (Springer Science & Business Media, New York).
73. Chen HL, Bian HT, Li JB, Wen XW, Zheng JR (2012) Ultrafast multiple-mode multiple-dimensional vibrational spectroscopy. *Int Rev Phys Chem* 31:469–565.
74. Chen H, et al. (2015) Vibrational energy transfer: An angstrom molecular ruler in studies of ion pairing and clustering in aqueous solutions. *J Phys Chem B* 119: 4333–4349.
75. Chen H, Bian H, Li J, Wen X, Zheng J (2013) Relative intermolecular orientation probed via molecular heat transport. *J Phys Chem A* 117:6052–6065.
76. Zhao Y, Truhlar DG (2008) The M06 suite of density functionals for main group thermochemistry, thermochemical kinetics, noncovalent interactions, excited states, and transition elements: Two new functionals and systematic testing of four M06-class functionals and 12 other functionals. *Theor Chem Acc* 120:215–241.
77. Andrae D, Haussermann U, Dolg M, Stoll H, Preuss H (1990) Energy-adjusted abinitio pseudopotentials for the 2nd and 3rd row transition-elements. *Theor Chim Acta* 77: 123–141.
78. Tomasi J, Mennucci B, Cammi R (2005) Quantum mechanical continuum solvation models. *Chem Rev* 105:2999–3093.

Downloaded from https://www.pnas.org by Peking University on September 3, 2022 from IP address 162.105.22.204.